Supplementary Information for:

MULTI-HAZARD ASSESSMENT OF THE EASTERN SLOPE OF THE SISTEMA DE FAMATINA, LA RIOJA PROVINCE (ARGENTINA)

Natural Hazards

Corbat, M. C. [1*]; Juárez, O.; Fucks, E.; Casas, J. A.

(1) Centro de Estudios Integrales de la Dinámica Exógena (CEIDE), Universidad Nacional de La Plata. Calle 1 n°644, C.P. 1900, La Plata, Buenos Aires, Argentina.

* E-mail address: mccorbat@fcnym.unlp.edu.ar

Table S1: Characteristics of the images collected over the study area

Satellite	Sensor	Acquisition date	UTC time	RGB composition	Target
Landsat 8	OLI	2016-07-18	14:26:16	5,4,3	Wildfires
		2016-08-03	14:26:19	7,5,4	
Sentinel-2A	MSI	2017-11-17	14:38:44	4,3,2	
		2017-12-12	14:37:31	8,4,3 12,8,4 12,11,4	
		2020-11-21	14:41:00	8,4,3	
		2020-12-11	14:40:57	12,8,4	
		2022-11-16	14:41:02	12,11,4	
		2022-11-26	14:40:59		
Landsat 4-5	TM	1991-10-18	13:50:27		
		2010-10-31	14:09:56	3,2,1	
Landsat 7	ETM+	2001-10-30	14:08:23		Population
Landsat 8	OLI	2022-11-24	14:26:50	4,3,2	
Terra	ASTER	2010-09-21	14:28:08	3,2,1	
		2019-01-01	14:29:01		
Landsat 8	OLI	2013-11-15	14:27:59	5,4,3	Plantations
		2017-02-15			
		2022-11-24	14:26:50		

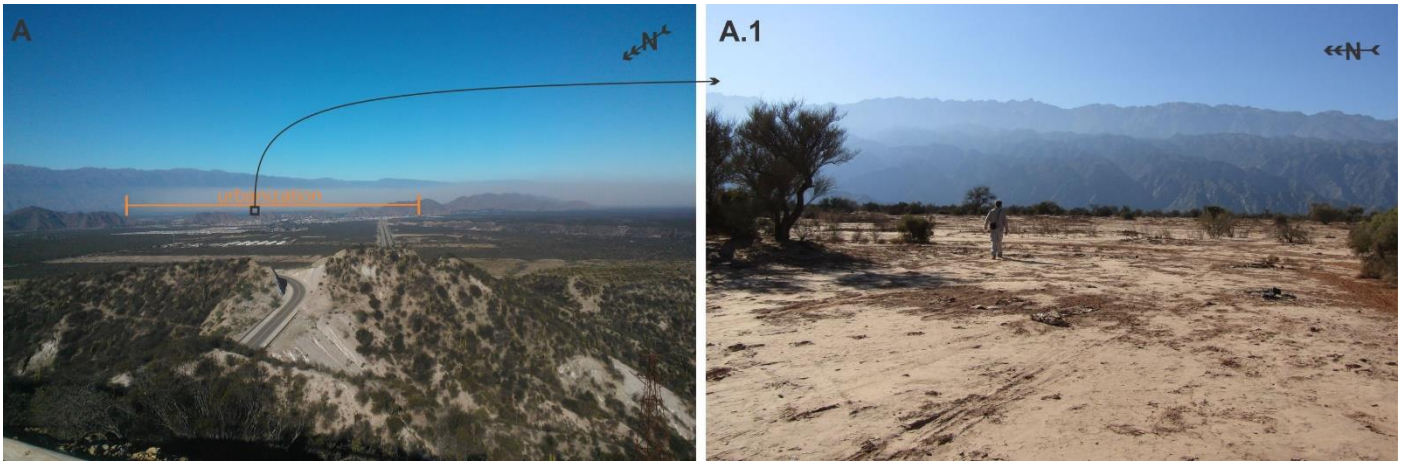

Fig. S1. Examples of aeolian activity and visibility reduction due to wind-entrained and suspended particulate matter. A) Southeast-facing view from cable-car station 2 toward the locality of Chilecito. A.1) Detail of a sector composed of silty-clayey materials (approx. 29°13’02”S / 67°21’18”W), with an eastward view. Scale reference: person (1.80 m).

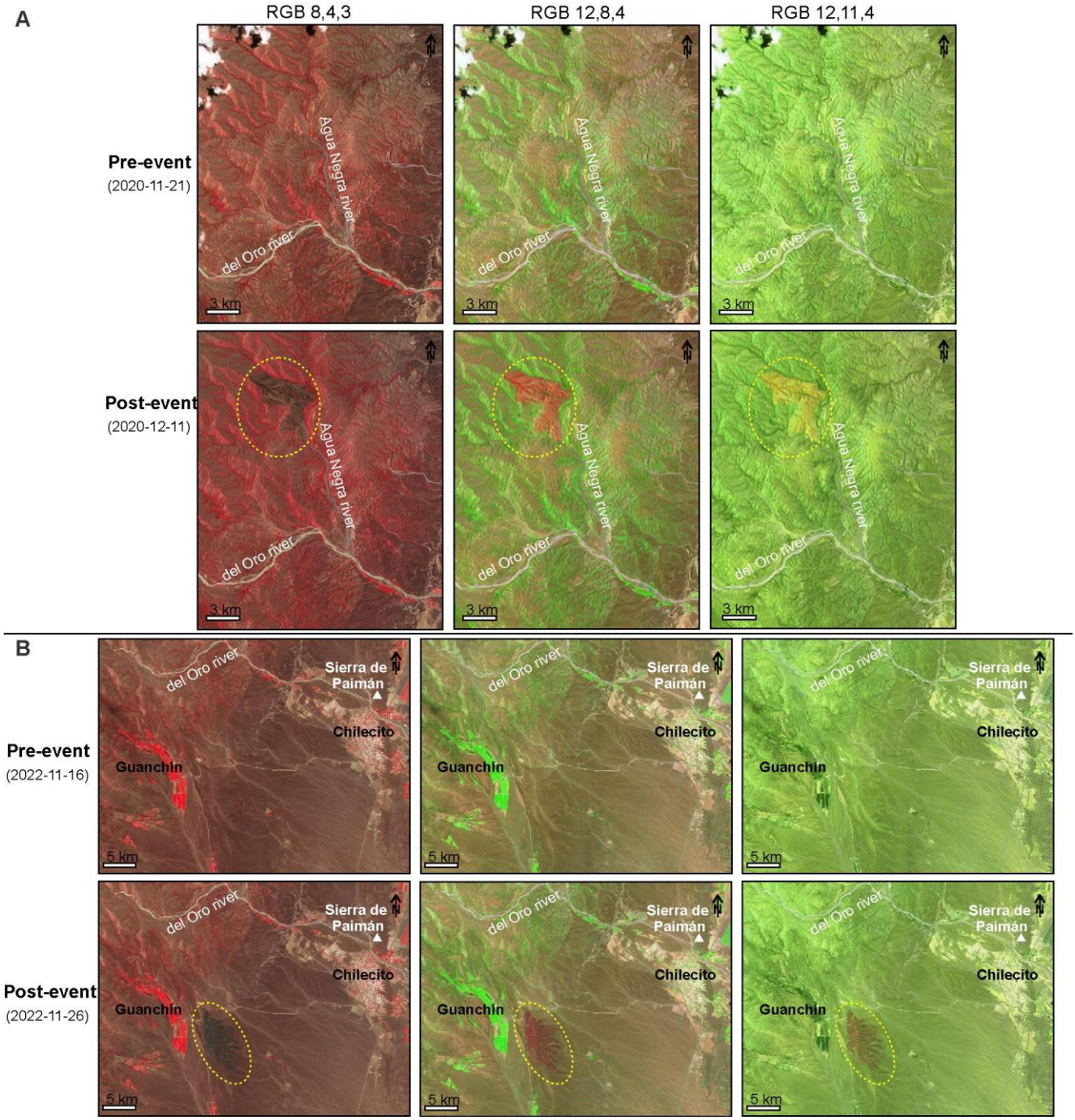

Fig. S2. Identification of fire-affected areas (indicated by dashed lines) based on Sentinel-2 satellite imagery, using different RGB band combinations. Top: pre-event images. Bottom: post-event images.

Fig. S3. A) Gully development in a sector with nearby infrastructure (approx. 29°11'03"S / 67°29'19"W). Airbus imagery sourced from Google Earth Pro (April 7, 2023). Locations of additional figures are indicated by the orange box (A.1–A.3) and the green box (A.4). The area affected by gully erosion is marked with a yellow circle. A.1 and A.2) Maxar Technologies imagery from Google Earth Pro, depicting pre-construction conditions. A.3) Airbus imagery from Google Earth Pro. A.4) Detail of the initial green box, showing structures within the gully-affected sector.

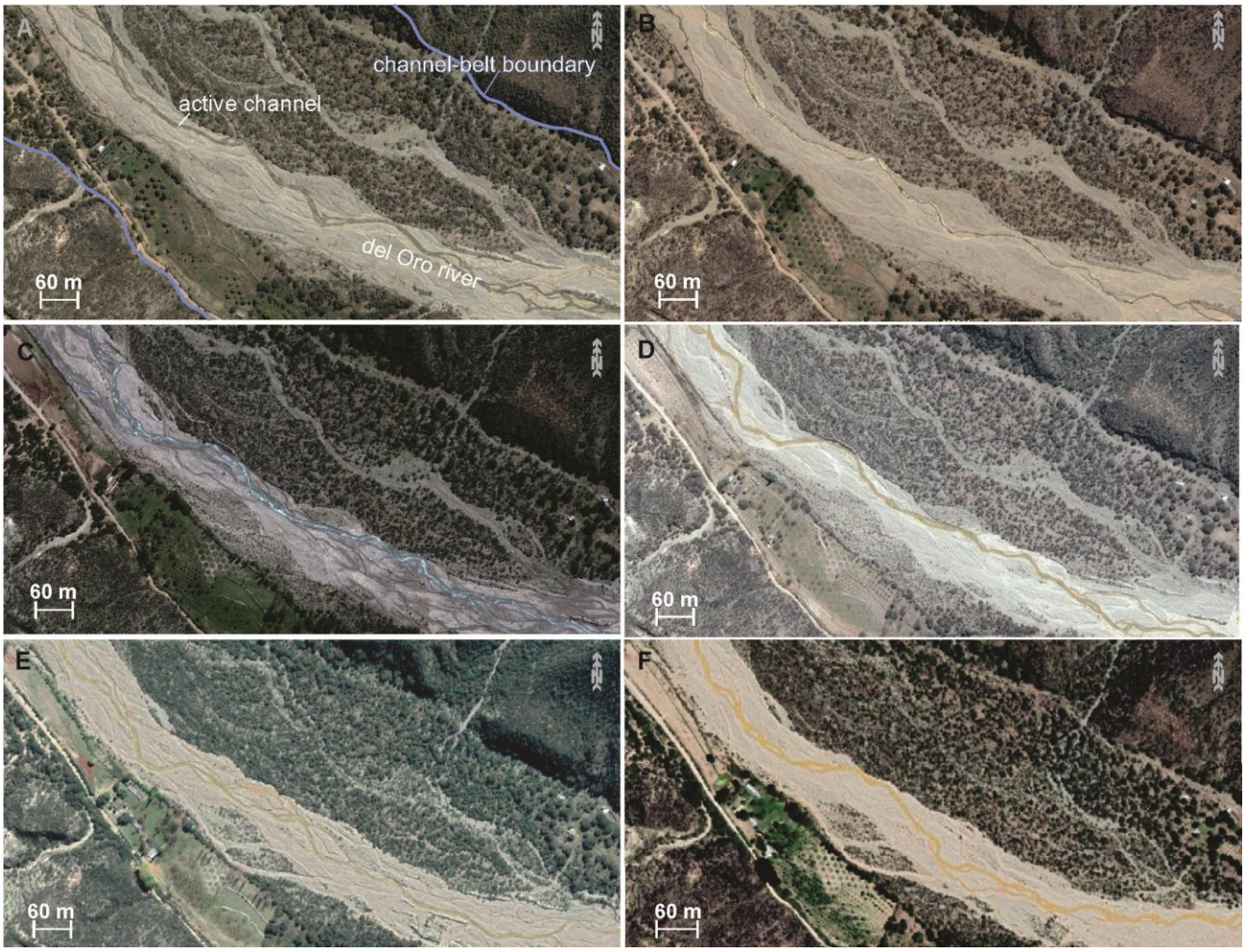

Fig. S4. Migration of the active channel of del Oro River. The analyzed sector is bounded by the coordinates 29°06’55”S, 67°35’15”W (upper left corner) and 29°07’13”S, 67°34’38”W (lower right corner). Maxar Technologies imagery obtained from Google Earth Pro for the following dates: A) April 17, 2004, B) October 14, 2004, C) March 9, 2011, D) September 23, 2013, E) May 12, 2019, F) November 22, 2022.

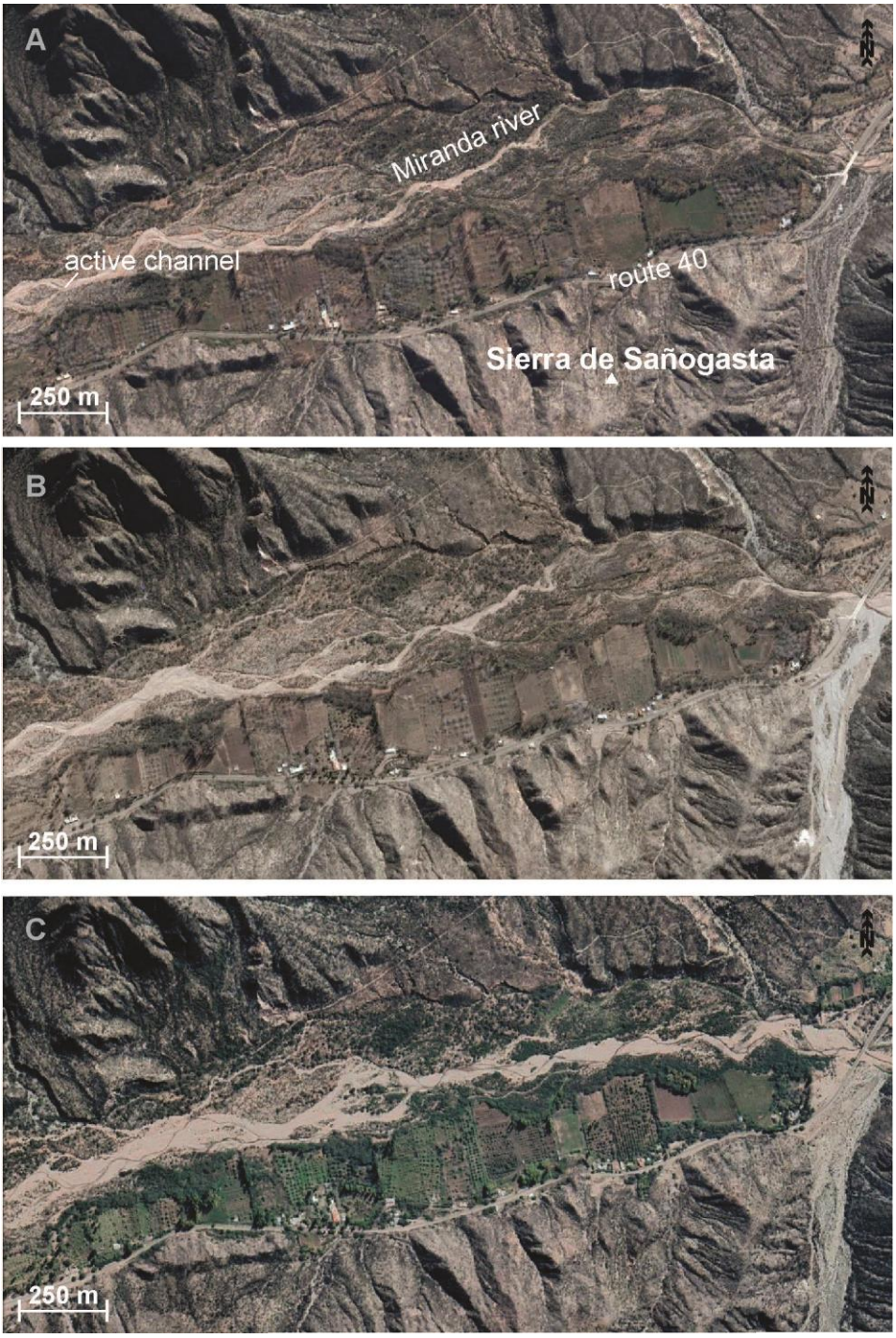

Fig. S5. Variations of the Miranda River. The study area is bounded by the coordinates 29°19′56″S, 67°40′45″W (upper left corner) and 29°20′37″S, 67°39′16″W (lower right corner). Maxar Technologies imagery obtained from Google Earth Pro for the following dates: (A) June 3, 2003; (B) July 19, 2013; and (C) May 9, 2021.

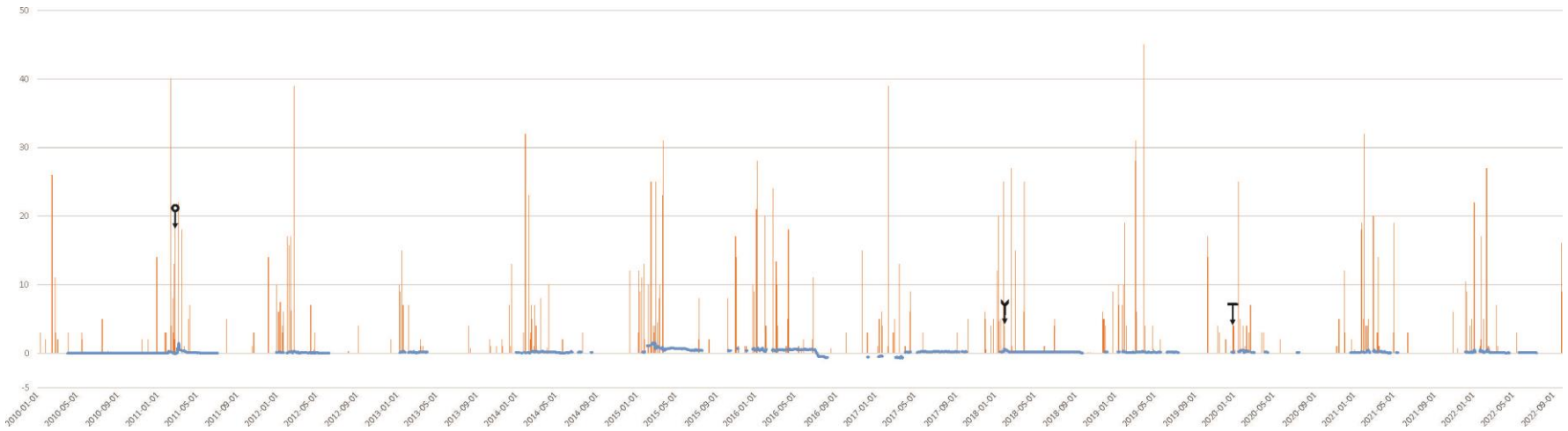

Fig. S6. Daily records of mean river stage (blue line) and precipitation (orange bars) for the period 2010–2022 at Chilecito. Arrows indicate, in chronological order, the following dates: February 25, 2011; January 31, 2018; and December 28, 2019. Source: Subsecretaria de Recursos Hídricos de la Nación (2018), Secretaría de Infraestructura y Política Hídrica de la Nación (2022), and Servicio Meteorológico Nacional (2018a, 2021, 2023a)

Fig. S7. Retaining structures associated with fluvial channels. A) Channelized segment of the Los Sarmientos River and adjacent urbanized areas. A.1) Braided channels, bars, and retaining structures (black arrow). View from the Sierra de Paimán (29°09'17"S / 67°29'19"W). A.2) Braided channels and coarse sediment bars. Active and inactive channels (29°09'09"S / 67°29'15"W). Urbanized area shown in orange. A.3) Retaining structures along the left bank of the Los Sarmientos River: concrete wall (gray arrow) and gabion structures (white arrow). A.4) Detail of retaining structure on the left riverbank (29°09'28"S / 67°28'26"W) showing basal degradation. A.5) Structure on the left bank affected by fluvial action (29°09'21"S / 67°28'40"W). A.6–A.7) Retaining structures on the right bank of the Los Sarmientos River: rigid wall (gray arrow) and gabions (white arrow). Urbanized area in the background (29°09'12"S / 67°29'06"W). A.8) Close-up of the structures shown in A.7 and their interaction with the active channel (29°09'16"S / 67°28'59"W). A.9) Detail of rigid wall (29°09'12"S / 67°29'10"W). B) Capayan River – gabion structures. C) Miranda River: 1) 29°20'09"S / 67°39'24"W; 2) 29°20'09"S / 67°39'22"W.

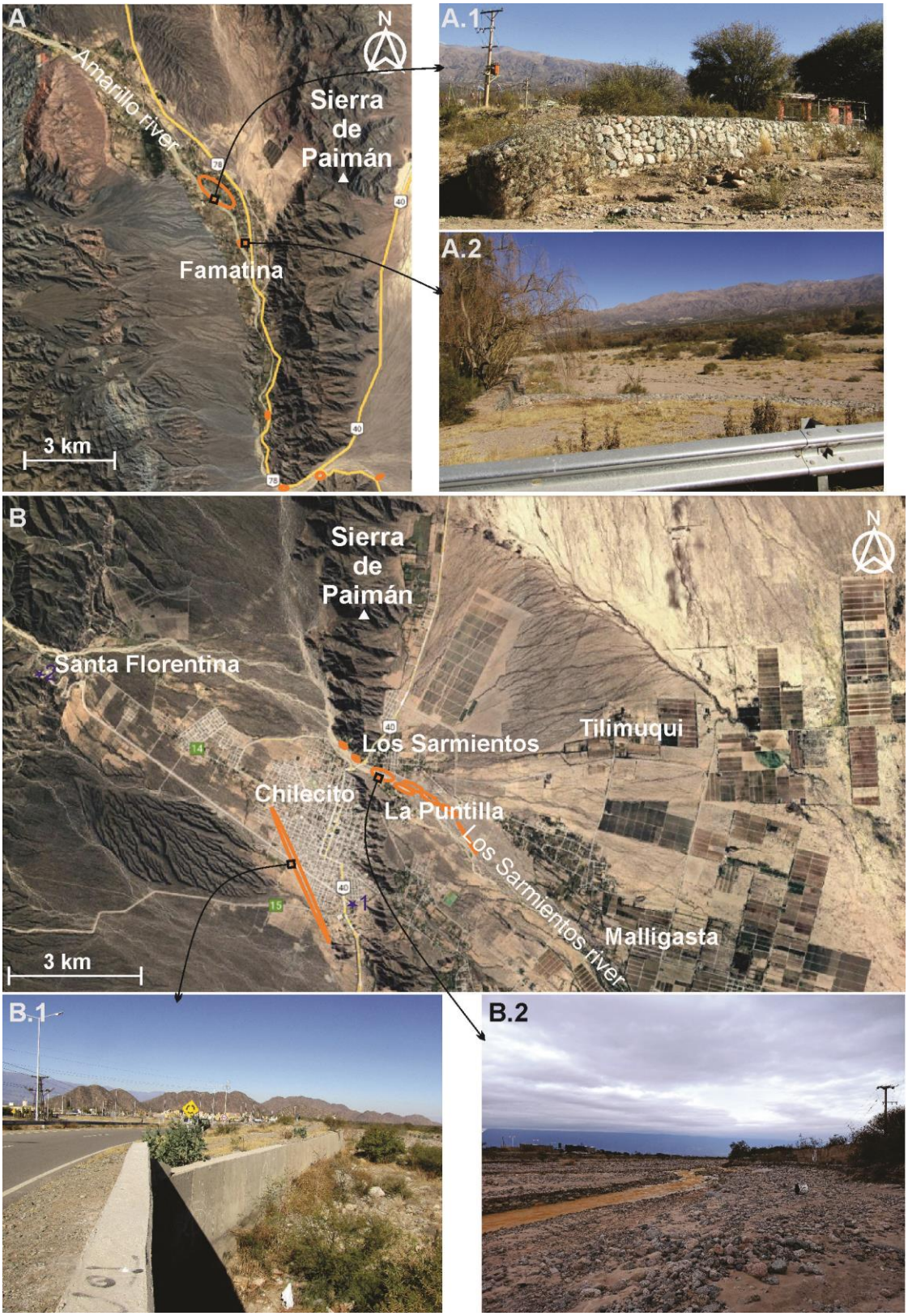

Fig. S8. Distribution of identified structures in orange-highlighted areas. A) Famatina area. Airbus image (February 9, 2023) sourced from Google Earth Pro. Associated photographs: (1) and (2). B) Chilecito area. Airbus image (July 9, 2023) sourced from Google Earth Pro. Locations of cable-car stations 1 and 2 are indicated by blue stars. B.1) Rigid structure bordering the southwestern perimeter of the Chilecito locality. B.2) Structural elements associated with the Los Sarmientos River.

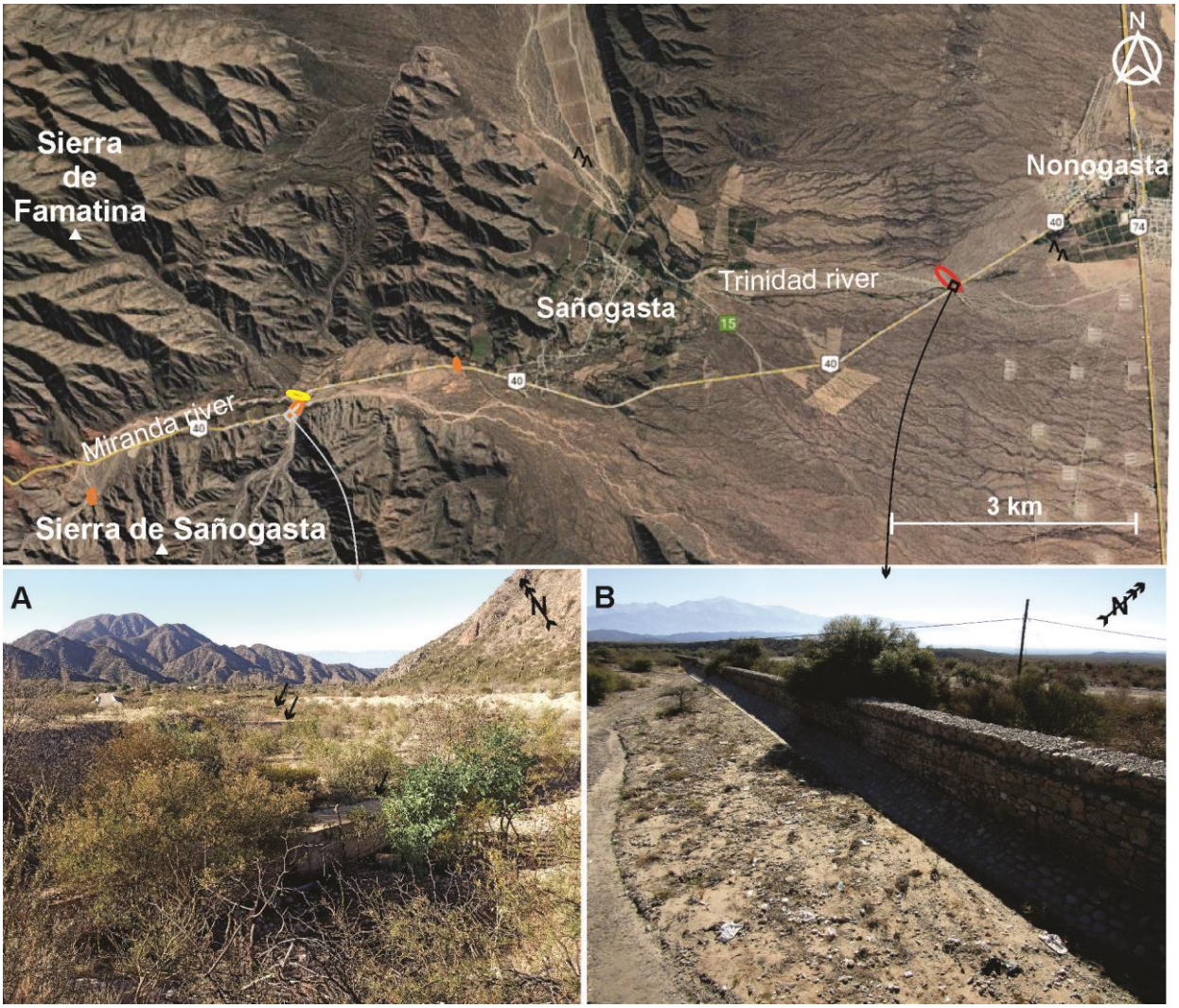

Fig. S9. Structures associated with fluvial channels influencing the localities of Sañogasta and Nonogasta. Location based on Airbus imagery (December 4, 2023), sourced from Google Earth Pro. Colors indicate the contributing watercourses associated with each structure: Miranda River (yellow), tributaries of the Miranda River (orange), and Trinidad River (red). Black inverted V-shaped symbols represent elevated linear accumulations of material. A) Photograph of structural elements (black arrows) along a tributary of the Miranda River (29°20’20”S / 67°39’25”W). B) Detail of a retaining structure associated with the Trinidad River (29°19’08”S / 67°32’22”W).

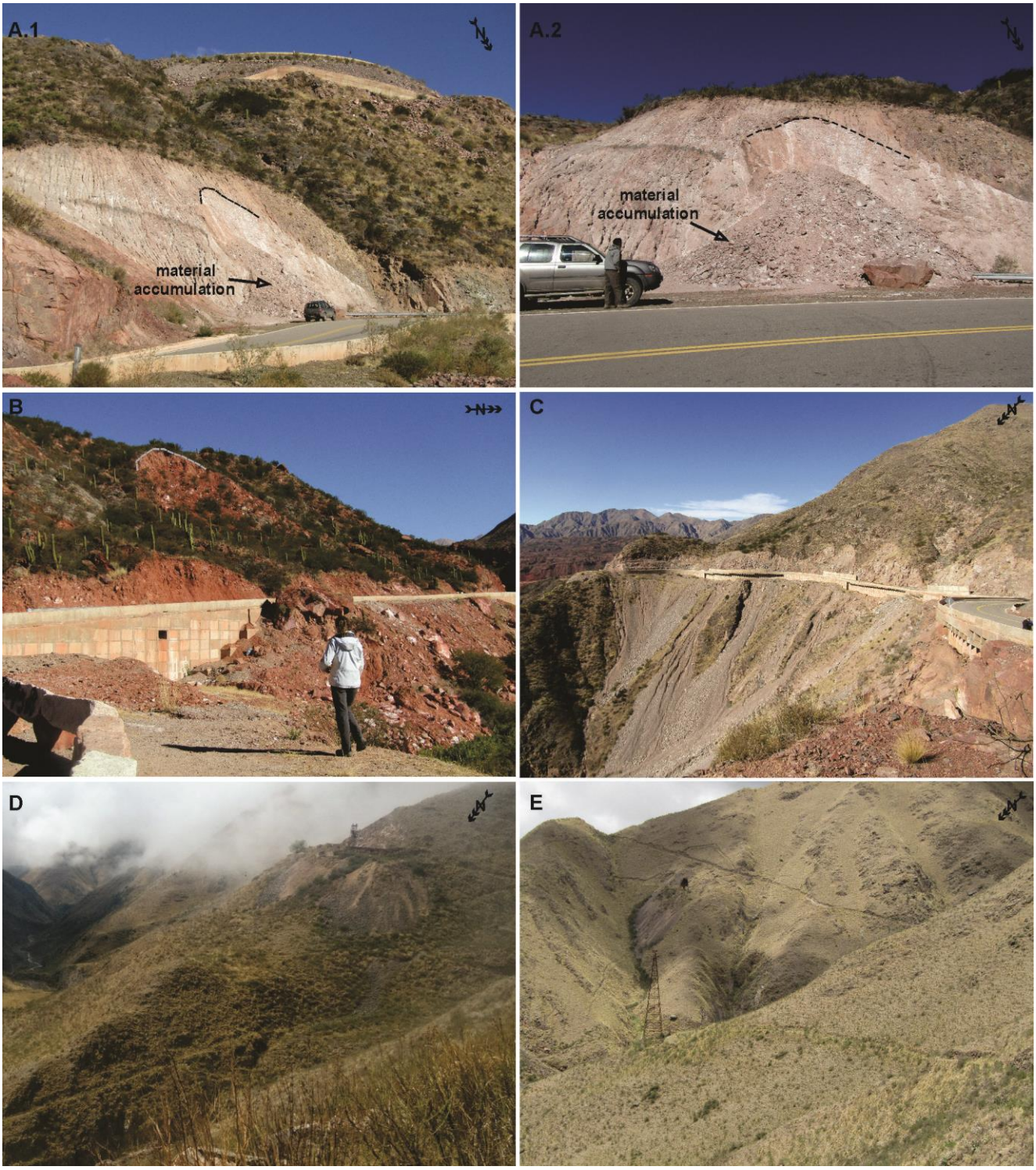

Fig. S10. Mass movement processes associated with anthropogenic activity. A) National Route 40, Cuesta de Miranda (29°20’28”S / 67°45’51”W). Combined evidence of rockfall and debris fall with landslide (landslide scar indicated by dashed line). Scale: van. Note the proximity of accumulated material to the route. B) National Route 40, Cuesta de Miranda (29°20’55”S / 67°42’14”W). Scale: person (1.65 m). Landslide features are also visible (landslide scar indicated by dashed line). C) National Route 40, Cuesta de Miranda (29°20’28”S / 67°45’48”W). D and E) Rock and debris falls associated with mining infrastructure near "Station 5" of the cable-car system (29°02’50”S / 67°40’53”W) and the tunnel (29°03’30”S / 67°40’12”W), respectively.

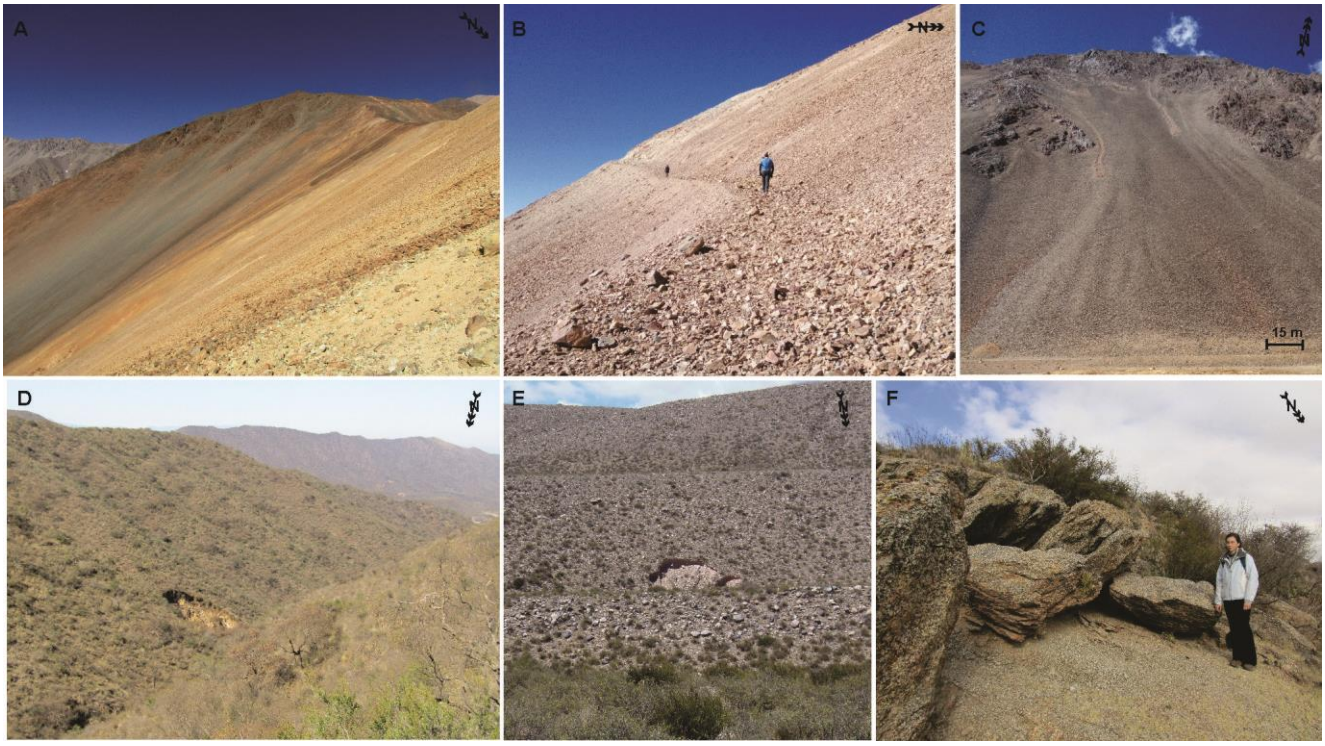

Fig. S11. Evidence of mass movement in the mountainous sector. A) Hillslope with rock outcrops, largely covered by loose debris (29°01’27”S / 67°46’00”W). B) Surface covered with a continuous mantle of debris (29°01’24”S / 67°45’59”W). C) Hillslope with exposed bedrock predominantly draped by debris; characteristic debris flow morphology is observed (light-coloured channels incised in the upper portions of the hillside). Photograph taken at 28°59’49”S / 67°44’08”W. D and E) Landslides identified by curved scarps, unvegetated surfaces and lack of surface material (D: 29°08’33”S / 67°39’17”W; E: 28°49’15”S / 67°42’15”W). F) Rock toppling sequence observed in the Sierra de Paimán (29°09’24”S / 67°29’15”W). Scale reference: person (1.65 m).

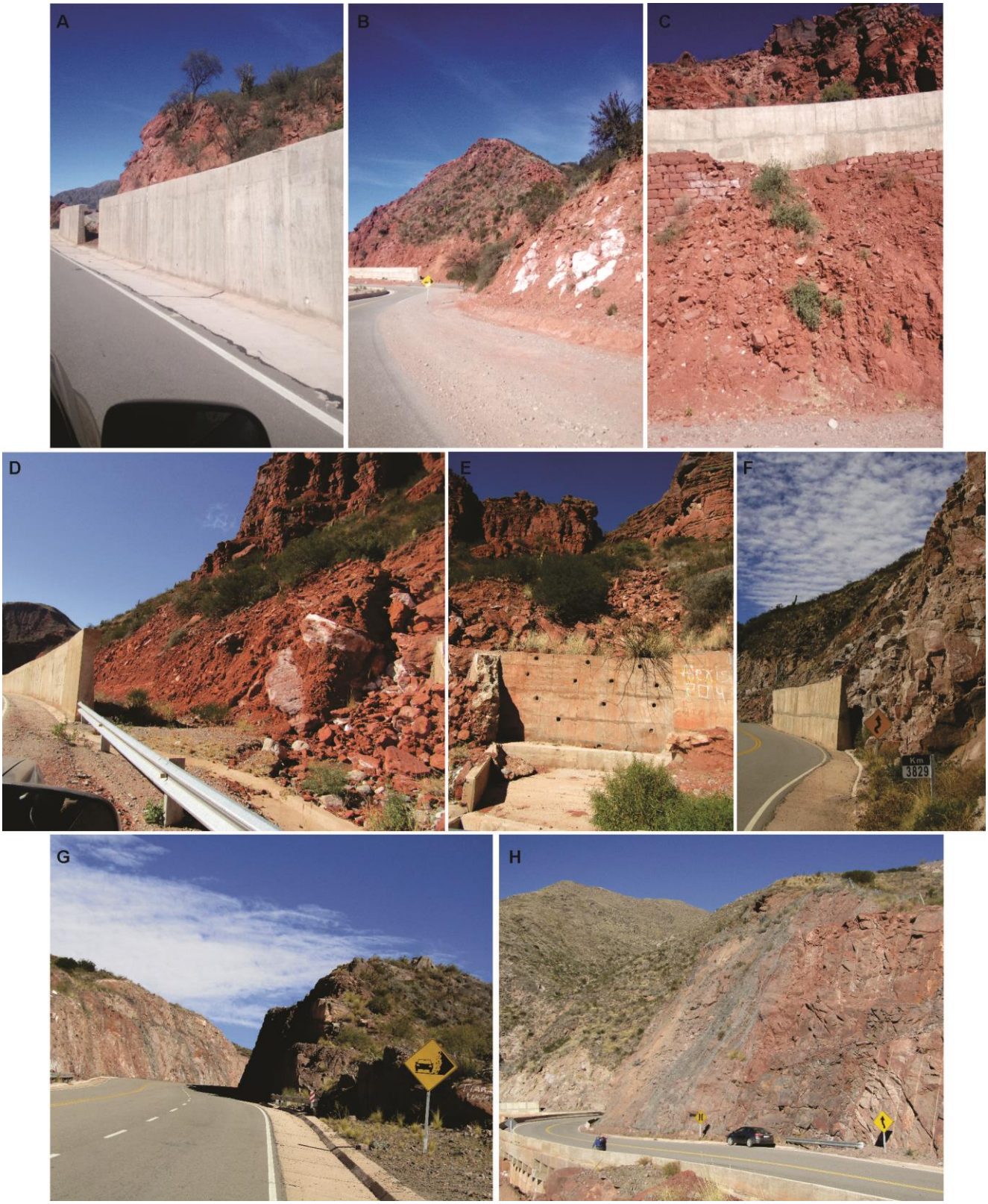

Fig. S12. Cuesta de Miranda. A–F) Concrete retaining walls (A–E: 29°20′47″S / 67°43′08″W; F: 29°20′38″S / 67°45′38″W). G) Warning signage indicating collapse-prone area. H) Slope stabilization structures consisting of a concrete retaining wall and wire mesh.

Fig. S13. Slope protection and retention structures. A–B) Retaining structures along Provincial Route 15 (29°10’58”S / 67°37’04”W). C) Wire mesh installed near the roof of a building along Provincial Route 12 (29°09’43”S / 67°29’04”W). D) Retention structure in the "El Rincón" neighborhood (29°10’19”S / 67°29’05”W). E) Warning signage indicating a collapse-prone area (29°05’53”S / 67°41’51”W).

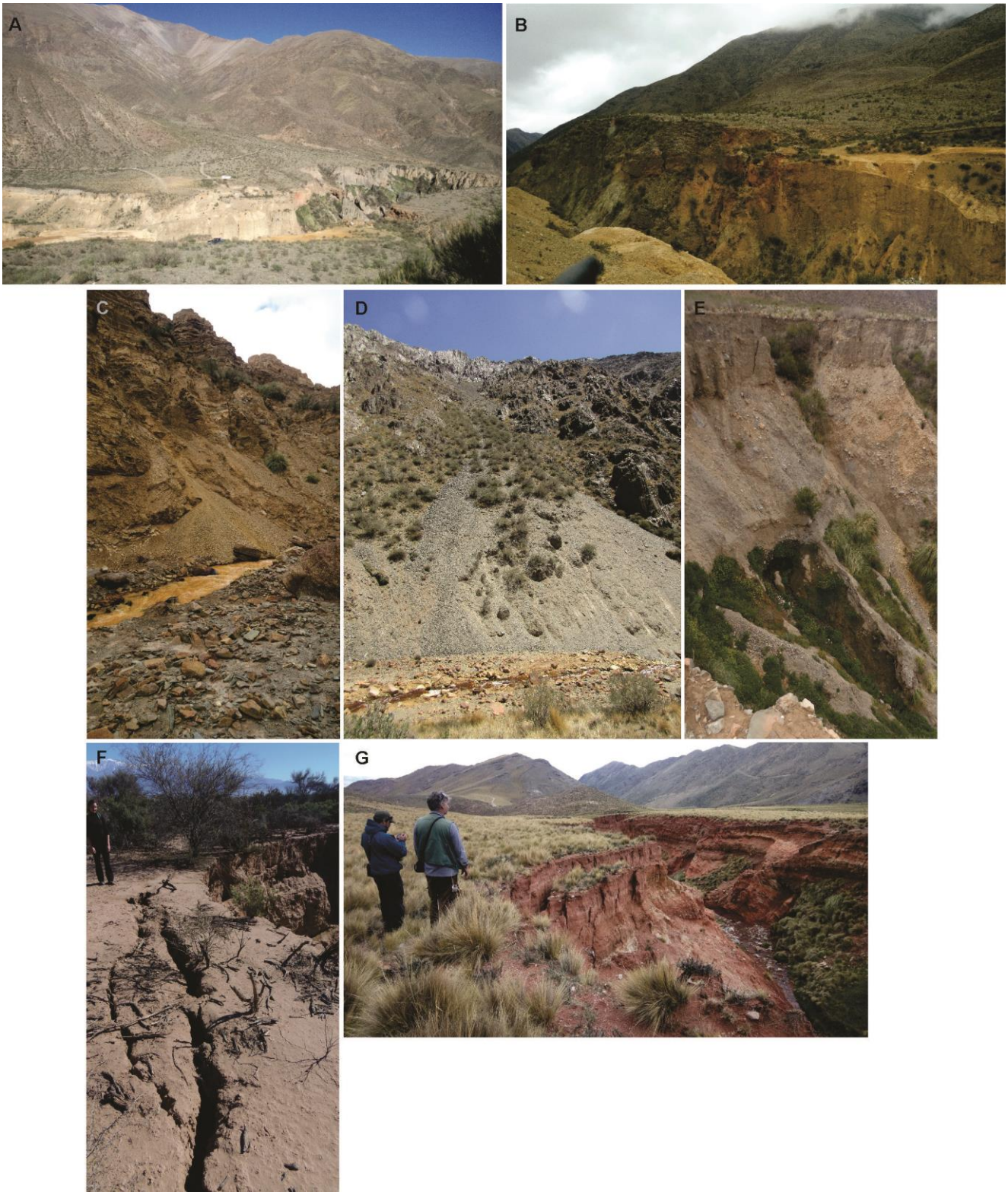

Fig. S14. Mass movement processes associated with fluvial systems. A–E) Evidence along the Amarillo River. A: 28°54′09″S / 67°41′08″W; B: 28°54′09″S / 67°41′15″W; C: 28°54′14″S / 67°41′12″W; D: 28°58′02″S / 67°42′06″W; E: 28°54′07″S / 67°41′15″W. F) Hazard due to cliff failure, collapse or toppling (29°11′25″S / 67°21′07″W). Scale reference: person (1.65 m). G) Tributary of the Achavil River (28°50′52″S / 67°46′41″W).

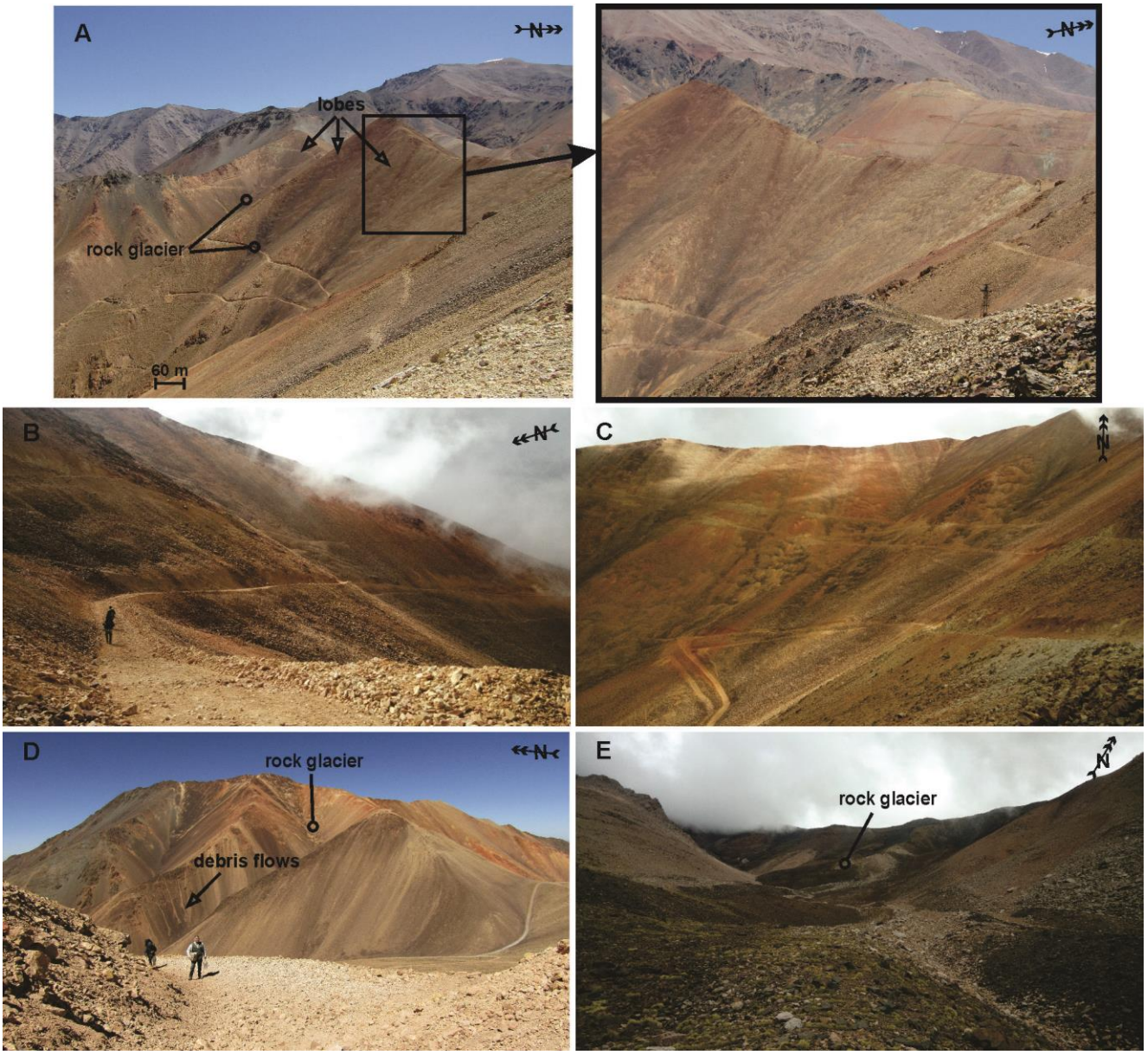

Fig. S15. Mass movement in a periglacial environment. A–C) Soli- and gelifluction features of varying dimensions located in the headwaters of del Oro River basin (29°01’08”S / 67°43’48”W). Inset in A: detail of lobes on the hillslope. D) Combination of soli-gelifluction features, rock glacier, and debris flows (29°01’03”S / 67°44’26”W). E) Hillslopes mantled with debris and the presence of a rock glacier (28°51’22”S / 67°48’45”W).

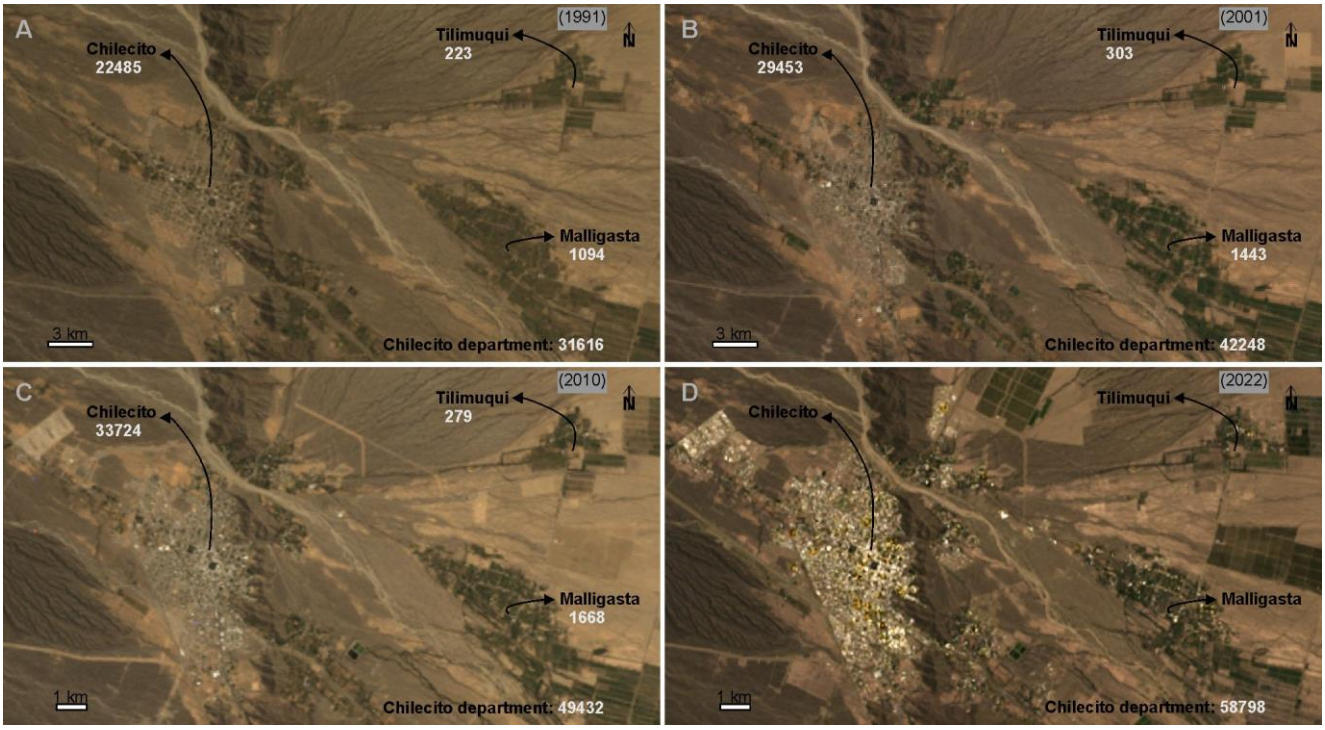

Fig. S16. Landsat satellite images illustrate the urban expansion surrounding the locality of Chilecito over 1991, 2001, 2010, and 2022, with built-up areas represented by white to gray tones. Population figures recorded in the corresponding national censuses are indicated for each year, highlighting demographic changes alongside spatial growth.

Fig. S17. An Airbus satellite image from April 7, 2023 (sourced from Google Earth Pro) showing constructions associated with the Los Sarmientos River, indicated by orange circles.

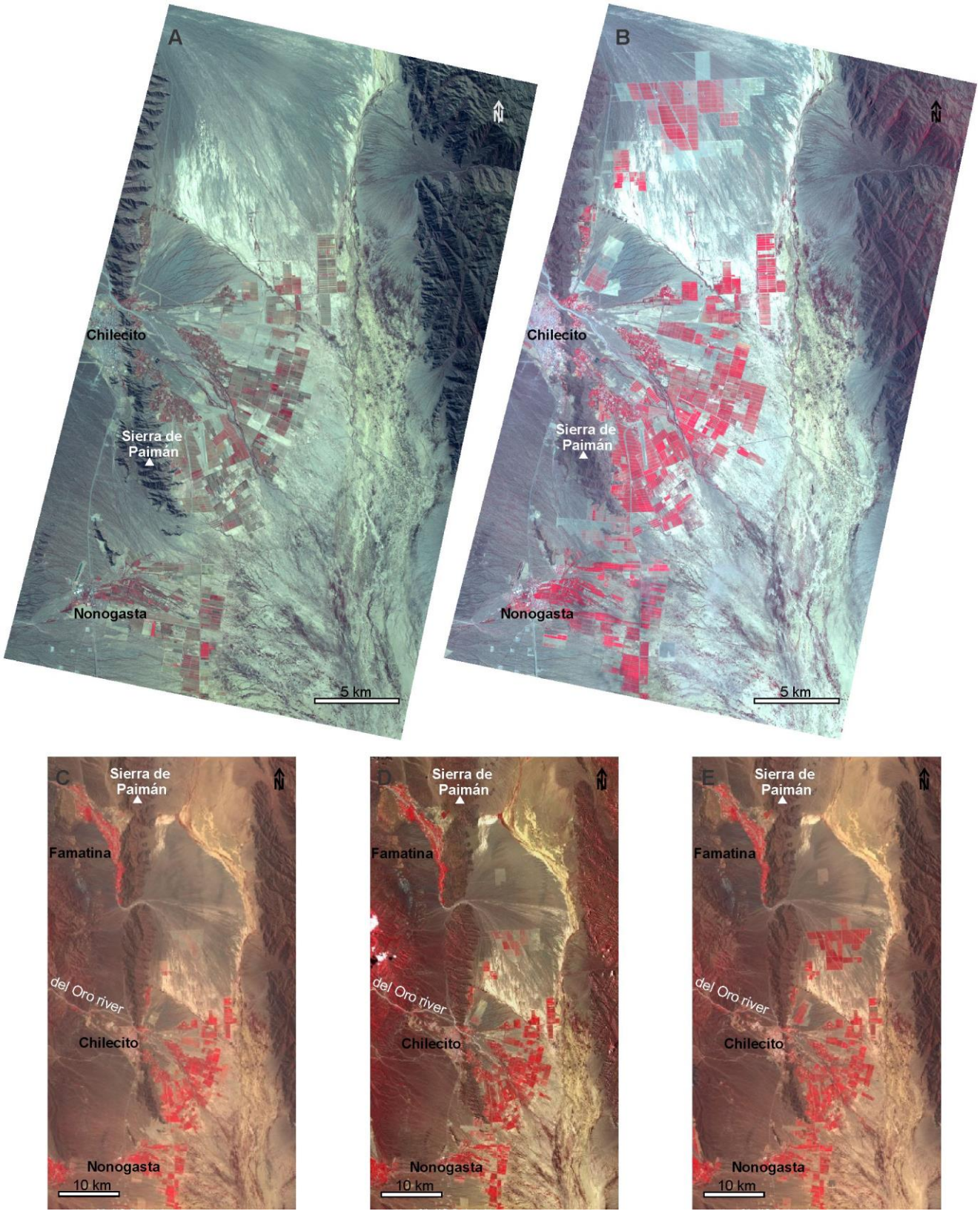

Fig. S18. ASTER (A, B) and Landsat (C, D, E) satellite images exemplify the expansion of plantation areas (highlighted by reddish polygons) using infrared-color composites. The images correspond to the years: (A) 2010, (B) 2019, (C) 2013, (D) 2017, and (E) 2022.

Fig. S19. Mining. (A) Precipitates associated with mining excavation draining into del Oro River. (B) Signage opposing mining activity at Avenida Pelagio B. Luna (29°09’24”S / 67°29’40”W), Chilecito. (C) Protest signage located at the bridge over the Capayán River.

Fig. S20. Anthropogenic interventions in the landscape. (A–C) Solid waste deposits associated with the road connecting the localities of Chilecito and Guanchín, primarily located along fluvial drainage pathways. (D–E) Disposal of agro-industrial waste observed in Airbus satellite images (September 7, 2023) from Google Earth Pro (D: 29°09′10″S / 67°28′34″W; E: 29°09′36″S / 67°23′08″W). (F) Photograph of graffiti at a mountain refuge (28°59′00″S / 67°44′00″W).

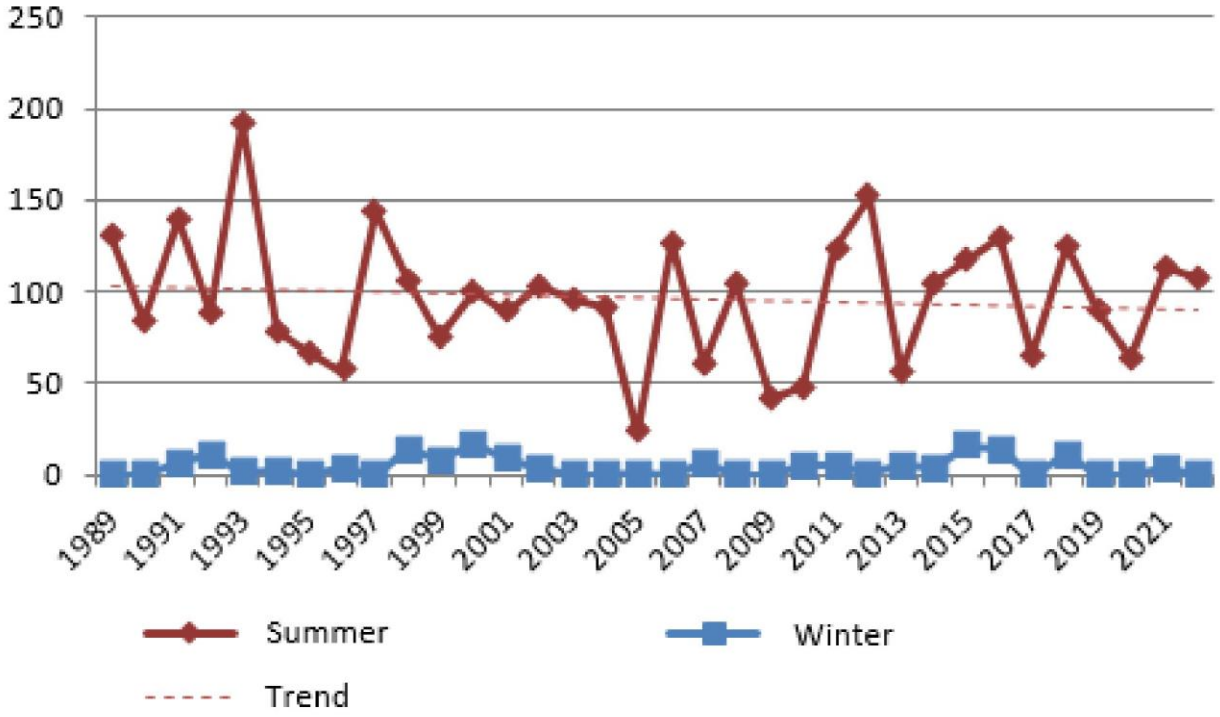

Fig. S21. Summer and winter precipitation totals for the period 1989–2022. The dashed line represents the overall trend in summer precipitation.

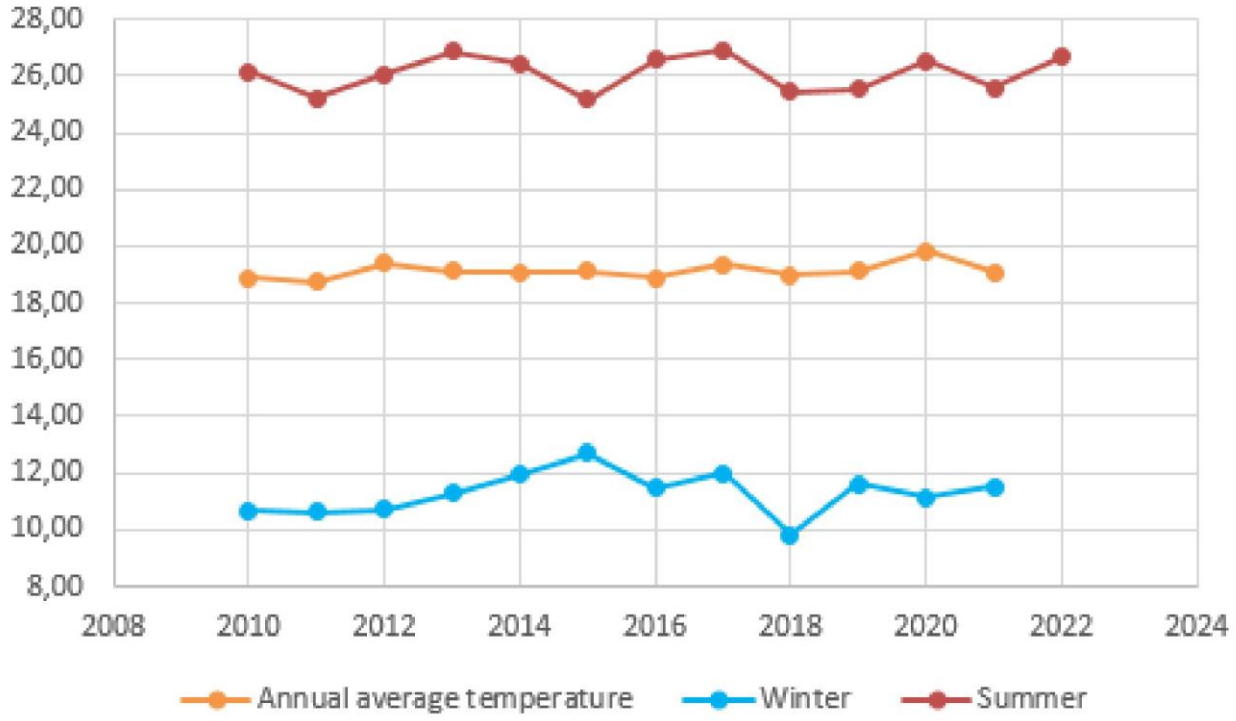

Fig. S22. Summer, winter, and annual mean temperatures for the period 2010–2022. The year 2020 stands out as the warmest within the analyzed interval. Temperature values are expressed in degrees Celsius (°C).

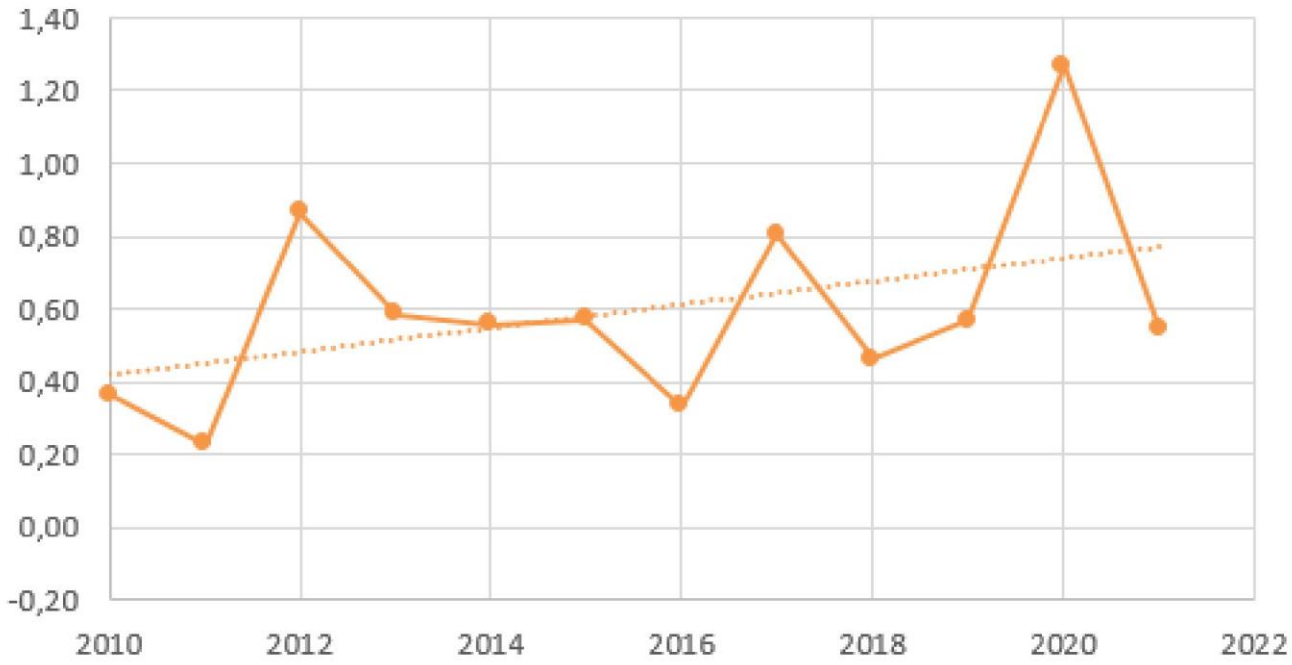

Fig. S23. Annual mean temperature anomalies for the period 2010–2022, expressed in degrees Celsius (°C). The baseline (0 value on the y-axis) corresponds to the average for the period 1991–2010. The dashed line indicates the overall trend in temperature anomalies throughout the analyzed period.

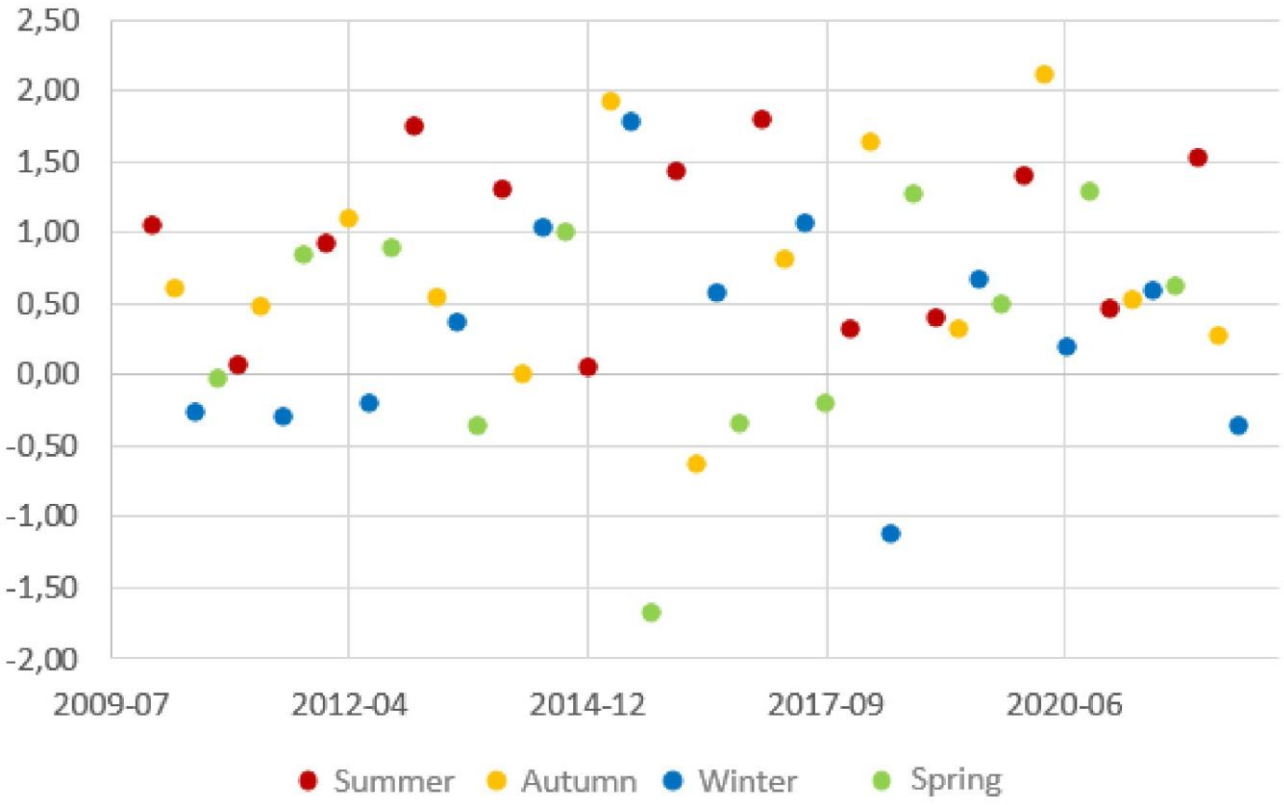

Fig. S24. Seasonal temperature anomalies for the period 2010–2022, relative to the avarage temperature for the period 1991–2010 (represented by the 0 value on the y-axis). Temperatures are expressed in degrees Celsius (°C).